Stall Development Control Using a Bio-Inspired Leading-Edge Design

Carlos Neves[⋆], *Caterina Gennari*[⋆] *and Raffaello Mariani*[⋆†]
[⋆]*KTH Royal Institute of Technology, Stockholm, Sweden*
Address
cneves@kth.se · gennari@kth.se · rmariani@kth.se
[†]Corresponding author

Abstract

This paper presents a numerical aerodynamic study of the stall characteristics and flow separation mechanisms of a blended wing body unmanned aerial vehicle being developed at KTH Royal Institute of Technology and proposes a bio-inspired leading-edge modification to control the separation mechanism and improve the aerodynamic performance of the aircraft at high angles of attack. A numerical study of the aircraft was performed at cruise speed, corresponding to Reynold's number of $1.3x10^6$, employing an Unsteady Reynolds Averaged Navier-Stokes solver with the Spalart-Allmaras turbulence model. Numerical results indicated that the aircraft is characterized by the presence of an unstable longitudinal vortex – visible at the stall angle of 9 deg – which breaks up at an angle of attack of 10 deg, resulting in an unsteady, full-chord stall cell in the mid-span region of the wing section. To mitigate this phenomenon, a modification to the leading edge between 0.4 m and 1.8 m wing spans was implemented inspired by the geometry of the nose of a porpoise whale, effectively generating a porpoise (hump) leading-edge inboard section. Preliminary numerical results indicate an increase in stall angle of attack to ∼13 deg and an in maximum lift coefficient to ∼1.0. Furthermore, the porpoise hump allowed controlling the stall behavior of the aircraft by enforcing a wing tip, trailing-edge separation stall achieved by the generation of an extended flow acceleration region at the leading edge.

1. Introduction

A blended-wing-body (BWB) flying demonstrator powered by a hybrid lithium-ion battery and by a hydrogen fuel cell is being developed[1] as part of a larger research effort at KTH Royal Institute of Technology in the field of sustainable future aviation. Previous aerodynamic studies of the aircraft have shown that the UAV has a low stall angle of attack and a maximum lift coefficient below a value of 1, in line with similar UAV designs.[1–3] These are undesirable aerodynamic characteristics that require assessment and improvement either by redesigning the wing or applying flow control techniques to modify the flow separation mechanisms on the aircraft.

The BWB design allows for the fuselage of an aircraft to be a lifting surface and thus largely improve its aerodynamic efficiency. However, the flow development about it differs from that of a conventional tubed fuselage aircraft at high angles of attack. The latter is shown by Dehpanah and Nejat[4] on their aerodynamic analysis of a moderately-swept wing BWB for its design optimization using computational fluid dynamics (CFD) based on Reynolds-Averaged Navier-Stokes equations (RANS) solvers. They found that even at low angles of attack, there's a gap between low- and high-pressure coefficients at the trailing edge of the BWB that produces vortices whose interaction with the wingtip vortex extracts energy from the flow and thus promotes flow separation.[4] Similarly, Panagiotou and Yakinthos[5] performed a parametric study using CFD of a highly-swept wing BWB concept in low subsonic conditions and observed that co-rotating vortical structures to the wing tip vortex, similar to the delta wing vortex system, are produced for a highly-swept BWB due to leading-edge separation at stall. These vortices produced at high angles of attack are due to the large nose and highly-swept inboard wing that generate a stable leading-edge vortex.[5] Conversely, common BWB and tapered wings with moderate sweep similar to that of the aircraft of reference are unable to produce a stable leading-edge vortex at high angles of attack. Nonetheless the cross flow induced by the swept geometry still leads to unstable leading-edge vortices that create large-scale recirculation regions causing stall at angles of attack below 12 deg as shown by Pavlenko et al.,[6] Wang and Zhou,[7] Ribeiro et al.,[8] and Neal et al.[9]

The experimental study of the flow features of a flying wing with moderate sweep at different angles of attack of Pavlenko et al.[6] showed that local full-chord, large-scale vortices onset at the wingspan sections close to the wingtip

at an angle of attack of 10 deg. This flow separation region further increases in size forming large recirculation regions over the wing at larger angles of attack. Similarly, Wang and Zhou[7] studied numerically and experimentally the flow separation mechanisms of a tapered, moderately-swept wing BWB. Both numerical and experimental results showed that the BWB experienced an abrupt, leading-edge separation at angles of attack larger than 8 deg where numerical results indicated flow separation onset at midspan wing sections in contrast to the wingtip flow separation onset observed experimentally.[7] Nonetheless, midspan flow separation onset is the one expected on moderately-swept, tapered wings as shown experimentally and through direct numerical simulations (DNS).[8, 9]

To control flow separation, passive and active techniques can be employed. The work of this paper focuses on passive flow control techniques given their application simplicity with respect to active flow control. Passive flow control devices consist on non-movable modifications of the aerodynamic surfaces that do not require energy input to modify the momentum of the boundary layer increasing the inertia of the flow to reduce the deceleration of adverse pressure gradients thus controlling the flow separation mechanism.[10] Since the aforementioned research on BWB describes an abrupt, leading-edge separation onset to be expected on moderately-swept, tapered wings such as that of the current aircraft configuration, the work of this paper focuses on leading-edge modifications to control separation. The latter is motivated on the fact that downstream pressure gradients on airfoils and wings are moderately sensitive to the leading-edge shape and thickness according to Mohammed and Yadav,[11] while popular passive flow control devices employed on aircraft wings such as vortex generators are better suited for controlling moderate to low adverse pressure gradients where the flow structures generated can further develop downstream (i.e. on a wing with moderate, trailing-edge flow separation).[12, 13]

Ma et al.[14] study was principally based on the optimization of the porpoise nose parameters by taking inspiration on the nose of other whale species. Their results have shown that the bio inspired leading edge modification to a NACA 2412 airfoil allowed modifying and increasing the surface area where the flow is accelerated at the leading edge with respect to the baseline airfoil. Consequently, a more energized boundary layer was produced on the leading-edge of the porpoised airfoil while displacing the stagnation point farther downstream on the pressure surface and increasing the aerodynamic efficiency at each angle of attack. This further allowed the stall delay while increasing the maximum lift coefficient with respect to the baseline airfoil.[14] The effects on the flow field and aerodynamic performance introduced by the porpoised airfoil are similar to those observed on race car wings whose leading edge is drooped and sharpened to increase the suction peak achieving a thinner boundary layer that delays upper-surface transition as described by Katz.[10] Nonetheless, the flight envelop of an aircraft comprises a larger range of angles of attack when compared to the wing of a race car, therefore a leading-edge modification requires a larger nose radius similar to a drooped nose of a high-lift device of commercial airliners to retain the stagnation point close to the leading edge.[10, 15, 16]

Following Mohammed et al.[14] research, Mohammed and Yadav[11] employed the optimum design of the leading-edge modification on infinite and finite wings with NACA2412 and NACA66215 cross-section at low-subsonic and high-subsonic regimes. They studied the flow separation control of the device with different spans at certain wingspan sections, forming a porpoised bump at the wing's leading edge. Their study showed that employing the porpoised bump at low-subsonic speeds and low angles of attack had negligible influence on the flow field. However, at higher angles of attack the larger flow acceleration extension on the porpoised bump produced a lower suction peak with a larger chordwise extent with respect to the baseline wing. Consequently, the large flow separation was suppressed while further producing a thinner wake with less turbulent kinetic energy henceforth increasing the stall angle of attack, the maximum lift coefficient, and the aerodynamic efficiency of the modified wing.[11]

The objective of this preliminary numerical work is to evaluate the aerodynamics of the reference aircraft and determine the flow separation mechanism near stall and to propose a passive method for controlling and delaying stall inspired by the nose of a porpoise whale. The leading-edge modification employed in this research is based on the nose of the porpoise whale nose shown in Fig. 1 (left) where the technical methodology is focused on the work performed by Momamed and Yadav[11] and Ma et al.[14] This geometric modification of the leading edge of the airfoil cross section of the wing is bounded to the nose length l_N, nose depth d_N, and nose diameter $\varnothing_N$, that are drafted from the LE diameter $\varnothing_{LE}$ center while following the nose profile of the porpoise whale as shown in Fig. 1 (right).

In this manuscript, Section 2 of this paper describes the numerical methodology. Section 3 discusses the aerodynamic results. Finally, Section 4 summarizes the study and provides insight into future work.

2. Methodology

The work was conducted using the commercial CFD software ANSYS Fluent where the fluid domain is discretized and the Navier-Stokes Equations are solved numerically. The flow conditions corresponded to cruise flight at different angles of attack at a Re of $1.314 x 10^6$. Therefore, the flow physics is dominated by turbulent phenomena modeled using steady and unsteady Reynolds-aAveraged Navier-Stokes equations (RANS/URANS).[18] The Spalart-Allmaras turbulence model was chosen to model the effect of the Reynolds stresses of the URANS. The Spalart-Allmaras is a
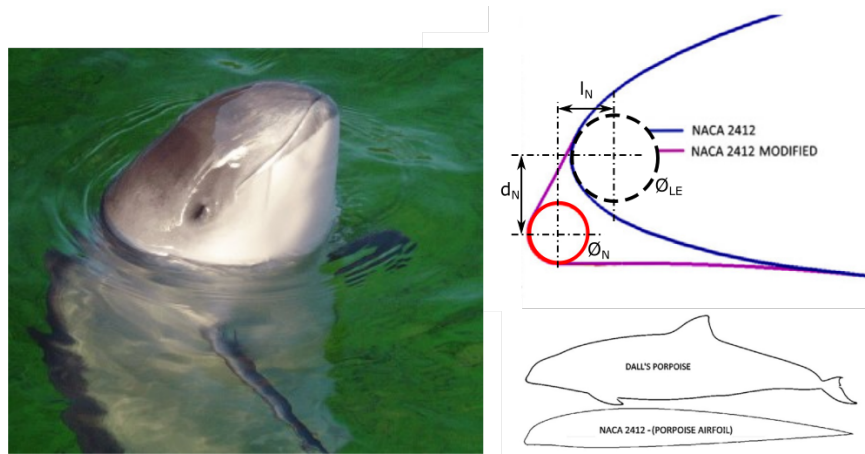
Figure 1: Porpoise whale nose[17] (left) and leading edge design[11] (right)

turbulence model that has been developed to provide a simpler, one-equation model to improve computational efficiency whose terms had been specifically tuned to model accurately flow separation in aeronautic applications.[19,20] The Spalart-Allmaras turbulence model has been chosen for this study since previous studies of the aircraft employed this model, showing satisfactory results validation, so as for other research on the optimization and aerodynamic analyses of BWB.[1,3,21,22]

The computer-assisted design (CAD) setup of the fluid domain used for CFD simulations of the 1:1 aircraft and the fluid domain are shown in Figure 2. The fluid domain enclosure corresponds to a box domain similarly to that employed by Suewetanakul et al.[1] Additionally, three volumes shown in Figure 2(a) are used as bodies of influence to control the mesh sizing around the aircraft and ensure a proper volume ratio transition between elements of the inflation layer and the far-field mesh.

The boundary conditions (b.c) employed correspond to symmetry boundary conditions at the symmetry plane of the aircraft and the plane parallel to it located outboard from the wing tip; non-slip wall on the aircraft surface; inlet boundary conditions corresponding to a freestream velocity of 20 m/s; and outlet boundary conditions of zero-gauge pressure normal to the outlet boundaries. Both inlet and outlet boundary conditions include turbulent boundary conditions corresponding to a turbulence intensity of 0.5% and a turbulent length of 0.0096 m. The location of boundary conditions is depicted in Figure 2 (b).

To decide on the refinement level of the mesh, three cases with different refinement levels (coarse, medium, refined) were generated following the Grid Convergence Method guidelines with the element size scaling between refinement levels corresponding to 1.3.[23] The mesh generated for the medium-level mesh corresponded to an unstructured mesh using tetrahedral elements with mean and maximum sizes of 0.87 and 1.5 m, respectively for a medium-level refinement. The defeature size was set to $1x10^{-5}$ m. The bodies of influence from larger to smaller volumes were set at an element size of 0.035, 0.025, and 0.01 m, respectively. The element size at the aircraft surface was set to 0.01 m and the minimum curvature size to $8x10^{-4}$ m. Finally, an inflation layer with a first element height of $3x10^{-6}$ m was set to ensure a y^+ value lower than 1. The growth rate and the number of layers of the inflation layer of the coarse, medium,
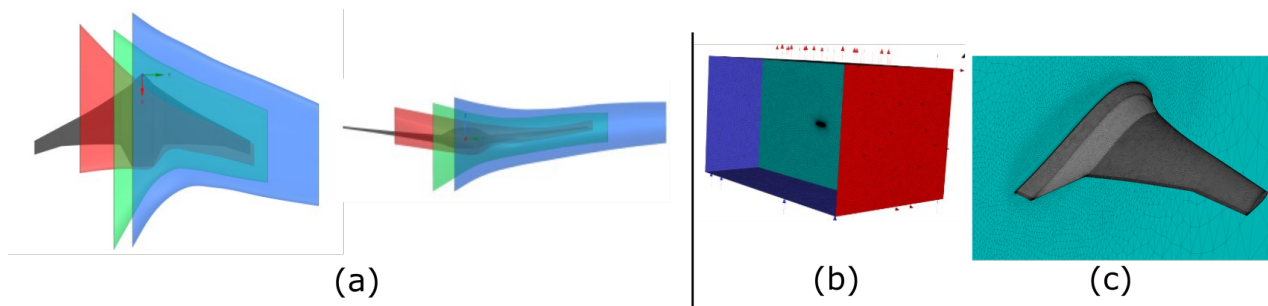

Figure 2: Numerical domain: (a) CAD setup of the fluid domain with the aircraft and bodies of influence details; (b) Fluid domain enclosure mesh showing inlets (blue), outlets (red), and symmetry plane (cyan); Mesh detail of the isometric view of the aircraft

STALL DEVELOPMENT CONTROL

Table 1: Grid convergence criteria of the clean configuration mesh

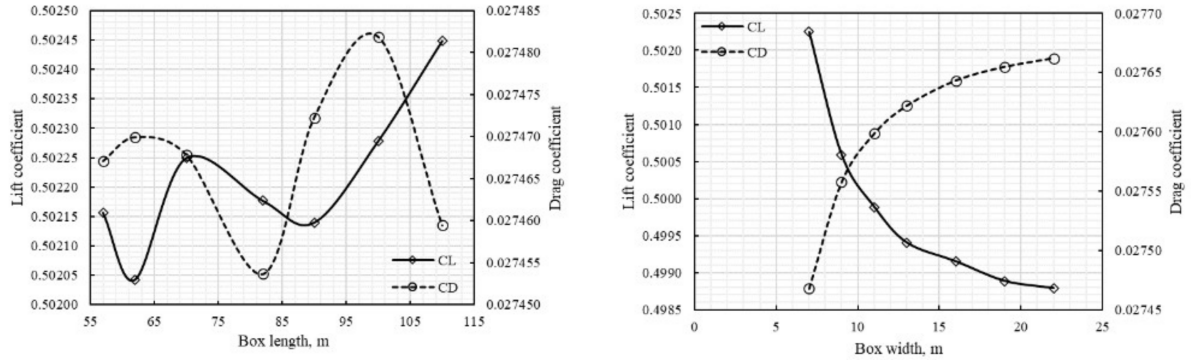|	p		$e_a\%$		$e_e\%$		GCI%	
	C_L	C_D	C_L	C_D	C_L	C_D	C_L	C_D
Coarse-Medium	3.53	0.14	0.11	0.51	0.39	2.14	0.49	2.14
Medium-Refined	3.53	0.14	0.05	0.53	0.16	1.75	0.19	2.23

Figure 3: Dependence of the aerodynamic coefficients to the fluid domain dimensions. Left: Aerodynamic coefficients variation with box length; Right: Aerodynamic coefficients variation with box width

and refined mesh were set to 1.2 and 44, 1.18 and 48, and 1.16 and 54, respectively. The resultant meshes for the coarse, medium, and refined levels were comprised of 5 780 477, 8 567 049, and 13 815 116 elements, respectively. The resultant mesh for the medium level is shown in Figure 2 (b-c).

The grid convergence study of the mesh generated was performed by simulating the clean configuration at an angle of attack α of 4 deg and using the Spalart-Allmaras turbulence model with steady RANS, pressure–coupled solver. Simulations were performed with second-order models for all the equations and the pseudo-transient approach for pressure coupling. The key variables chosen for the grid convergence study were the lift and the drag coefficient. All simulations achieved residual values on the order of magnitudes below 10^{-6} upon the convergence of the aerodynamic coefficients, except for the continuity equation. The continuity equation of all simulations achieved a residual value on the order of magnitudes below 10^{-3} upon the convergence of the aerodynamic coefficients. Additionally, a maximum y^+ value of 0.368 was obtained. The lift and drag coefficients obtained using the medium refinement level were 0.5020 and 0.02747, respectively.

The apparent order of the methods, the extrapolation and absolute errors, and the GCI between refinement levels were obtained according to the Grid Convergence Method guidelines.[23] The results of these variables are contained in Table 1. It's seen in Table 1 that the GCI between the medium and refined levels for the lift coefficient are 0.49% and 0.19%, respectively. Similarly, the CGI between the medium and refined levels for the drag coefficient is 2.14% and 2.23%, respectively. Besides, all the computed errors between refinement levels for both aerodynamic coefficients are below 2.2%. Hence, the usage of the medium refinement level mesh for aerodynamic analyses is appropriate.

Upon deciding on the grid refinement level of the fluid domain, two additional grid convergence analyses were performed by studying the change of aerodynamic coefficients, one with respect to the length and height of the box domain and the other to its width. According to Goetten et al.,[24] the aerodynamic coefficients change with the extent of the fluid domain in such a way that the lift coefficient increases, and the drag coefficient decreases as the fluid domain volume increases. Figure 3 (left) shows the change of lift with box length (considering that the height of the box is twice its length always) and it's observed that the lift and drag coefficients change non-monotonically as the box length and height increase. Nonetheless, the change of the coefficients value with domain length and height is almost negligible on the fourth significant digit and thus a box with a length of 70 m is a suitable dimensioning for the fluid domain.

Additionally, Figure 3 (right) shows that the lift coefficient decreases and the drag coefficient increases as the box width becomes larger. Since the face parallel to the symmetry plane of the aircraft outboard from the wingtip is modeled as a symmetry plane, the setup corresponds to two aircraft in tandem formation. Therefore, increasing the box width corresponds to increasing the spanwise distance between both aircraft. Figure 3 (right) shows that the aerodynamic effects of such formation on the aerodynamics of the aircraft vanish when the box width is 22 m (i.e. when both aircraft are separated by 44 m). Hence, the box width for the aerodynamic study is set to 22 m.
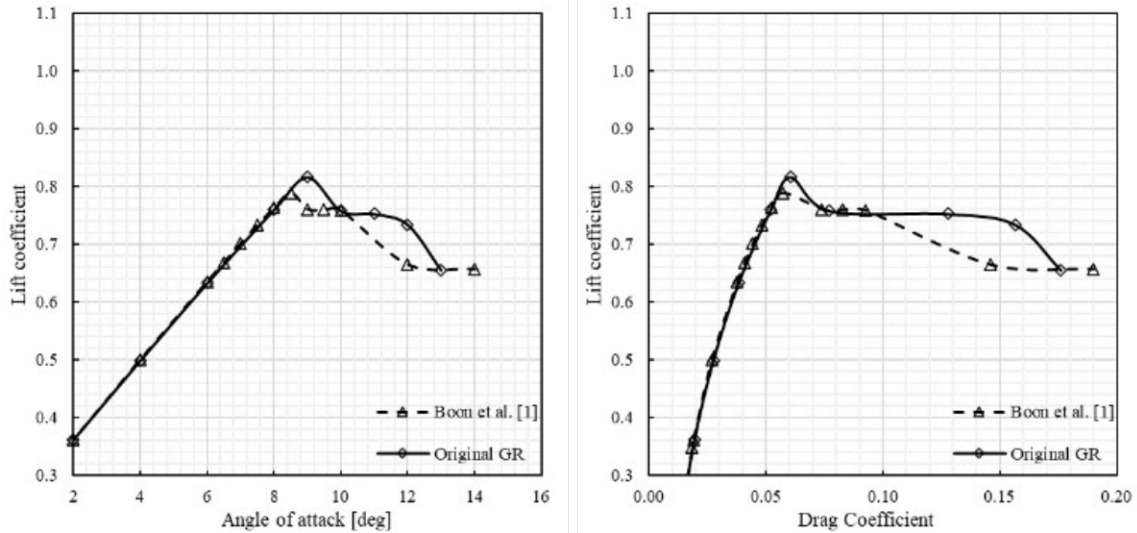
Figure 4: Aerodynamic characteristics of the baseline configuration

3. Results

A numerical analysis of the baseline configuration of the aircraft of reference was conducted at at the design cruise Reynolds number of $1.31x10^6$ to evaluate the overall aerodynamic performance, to determine flow separation mechanism of the aircraft, and to visualize the transient stall cells at high angles of attack. Once these conditions have been analysed, the study proceeds to assess the effects of the bio-inspired leading-edge modification on the stall development of the aircraft and further compares it to that of the baseline design. Studies were performed using both RANS and URANS approaches where the steady formulation was employed at low angles of attack and then switched to URANS when variations of the aerodynamic coefficients through the iterative procedure resulted using the steady solver at high angles of attack. The time step Δt employed for the URANS simulations corresponded to a value of $\frac{\Delta t U_\infty}{c} = 0.025$ as recommended by Li et al.[25]

3.1 Baseline Configuration

Numerical simulations of the baseline configuration were conducted at the cruise Reynolds number of $1.31x10^6$ for angle of attack of $-6 \ deg \leq \alpha \leq 13 \ deg$ to determine the performance of the aircraft, and obtained results have been compared with those obtained by Suewatanakul et al.[1] as shown in Figure 4. A small discrepancy of 0.5 deg is noticeable in the stall angle of attack and a difference of $\sim 3\%$ in maximum lift coefficient which may result from the differences in domain structure and increased number of cells in the area in close proximity to the aircraft and may be considered negligible. Figure 4 shows that the lift coefficient curve becomes nonlinear for α higher than 7 deg and the α_{stall} is seen to be equal to 9 deg where the $C_{L_{Max}}$ attained is 0.8166. Besides, the aerodynamic coefficients become fully unsteady varying below a deviation of 2% across the average value reported in Figure 4 for α larger than 9 deg. It's further seen in Figure 4 that the C_L starts to moderately reduce after stall for the angles of attack studied.

To support the study of the stall development and flow separation mechanisms of the baseline aircraft during cruise conditions, Figure 5 presents the λ_2-criterion isosurfaces with a pressure coefficient colormap limited to C_P values between -4 and 0 for better identification of suction regions. The λ_2-criterion isosurfaces provide a representation of vortex cores and separation regions.[26] Additionally, streamlines embedded to the λ_2-criterion isosurfaces and skin friction lines to the aircraft surface are presented in Figure 5. It's observed in Figure 5 that trailing edge flow separation has developed close to the wingtip at $\alpha = 9 \ deg$ forming a recirculation region that merges with the trailing vortex producing boundary layer cross flow that reduces the streamwise momentum of the boundary layer. Hence, the role of the strong wingtip vortex on decreasing the streamwise momentum to promote flow separation is shown as described by Dehpanah and Nejat.[4] Moreover, the recirculation region spans until a midspan wing section forming a vortex rib extending upstream. The position of this vortex rib serves as an indication of where large recirculation structures will develop along the span once the angle of attack keeps increasing, and indeed the stall onset occurs at midspan due to an abrupt leading edge flow separation when the angle of attack increased to 10 deg as observed in Figure 5 (right).
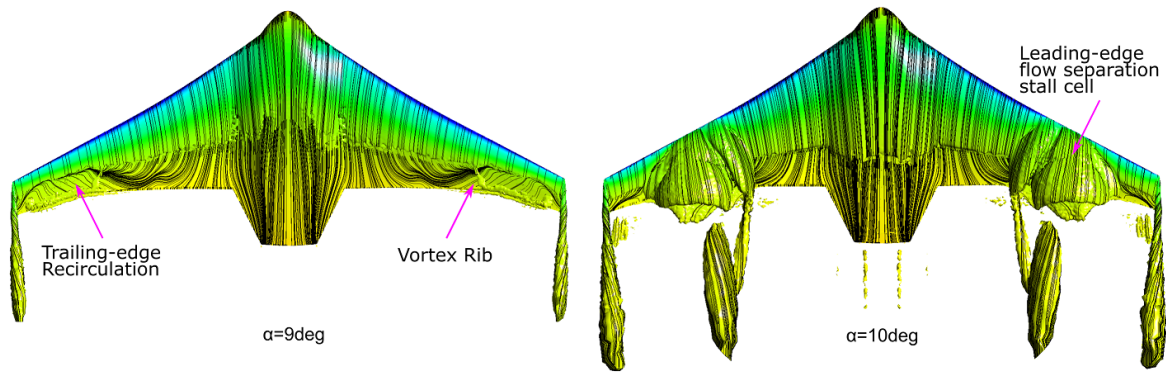
Figure 5: λ_2-criterion isosurfaces (pressure coefficient) of the baseline configuration at $\alpha = 9 \, deg$ (left) and $\alpha = 10 \, deg$ (right)
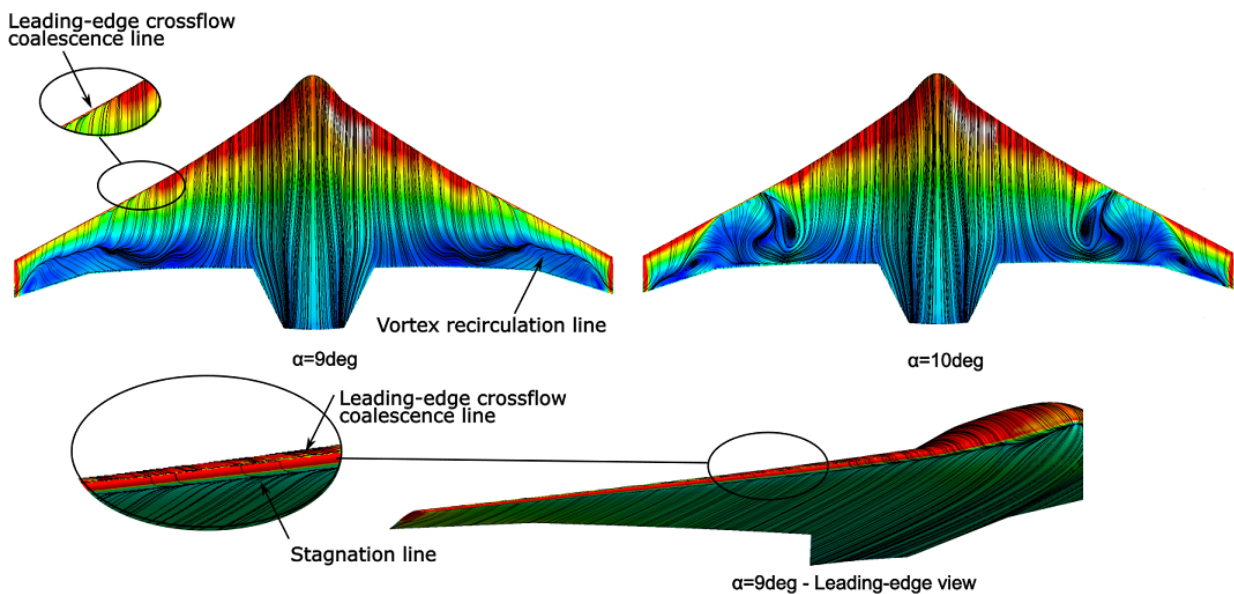

Figure 6: Skin friction contours and lines of the baseline configuration $\alpha = 9 \, deg$ (top left) and $\alpha = 10 \, deg$ (top right) with leading-edge inspection at $\alpha = 9 \, deg$ (bottom)

Midspan flow separation is a natural flow mechanism that onsets stall on swept-back, tapered wings as explained by Ribeiro et al.,[8] Neal et al.,[9] and Dias.[27] According to them, midspan flow separation is attributed to the simultaneous effects of the reduction of the local Re along the span due to the taper and the spanwise distribution of the downwash induced by the trailing vortex. As the chord along the span becomes smaller towards the wingtip, the stall of local wingspan sections occurs at a lower local angle of attack. However, the downwash induced by the trailing vortex increases along the span towards the wingtip thus the local angle of attack also reduces along the span towards the wingtip. Nonetheless, there's a wingspan section located midspan whose local angle of attack matches the stall angle of attack at the local Re, which is a lower stall angle of attack than that of stall-resistant but larger than that of wingtip wingspan sections that have a considerably lower local angle of attack due to the trailing vortex downwash distribution. Hence, the flow separation mechanism visualized in Figure 5 for the baseline configuration.

Further insight on the flow mechanisms that lead to flow separation during stall for the baseline configuration can be attained by studying the skin friction contours presented in Figure 6. It's observed in Figure 6 (top left) that the trailing edge flow separation developed at $\alpha = 9 \, deg$ is limited by a vortex recirculation line on the regions of low C_f as expected, causing an aggressive outboard crossflow on the lower layers of the boundary layer at midspan wing sections. This boundary layer crossflow at midspan wing sections extends upstream until the leading edge where it's seen that the boundary layer acceleration decreases considerably outboard along the span, even though suction is maintained along the entire wingspan as observed in Figure 5. The loss of the boundary layer streamwise inertia due to the crossflow makes the boundary layer sufficiently unstable at midspan sections causing the abrupt leading edge flow

separation once the angle of attack is increased to 10 deg as shown in the larger vortical structures observed in the low C_f regions of Figure 6 (top right).

Further inspection of the flow topology at $\alpha = 9\ deg$ on the leading edge can be observed in the close-up view presented in Figure 6 (bottom). It's observed in Figure 6 (bottom) that the stagnation line at $\alpha = 9\ deg$ is located on the lower surface of the wing and that the skin friction lines that bifurcate to the upper surface indicate that the flow at midspan wingspan sections crosses the leading edge by immediately forming a coalescence line on the upper surface given the strong crossflow in the boundary layer close to the wall. Therefore, this is an indication that the geometry of the leading edge at midspan wing sections needs a redesign to avoid the early boundary layer crossflow that deters the inertia gain of the flow at the leading edge of the wing.

3.2 Bio-Inspired Leading-Edge Configuration

Following the verification of the CFD setup and the study of the stall onset of the aircraft in section 3.1, it has been shown that the stall characteristics of the UAV are undesirable. Consequently, a leading edge-modification consisting of a bio-inspired design of a porpoise whale nose has been implemented to suppress the undesired midspan, leading-edge stall, and further achieve a wingtip, trailing-edge stall. The geometry is described in Section 3.2.1 and aerodynamic performance is discussed in Section 3.2.2

3.2.1 Geometry Definition

The geometrical characteristics of the porpoise nose included in the baseline aircraft configuration correspond to the optimum estimated by Mohammed and Yadav[11] for the NACA2412 and NACA66215 airfoils consisting of a porpoise nose diameter of 0.02c, a porpoise nose depth of 0.0225c, and a porpoise nose length of 0.0075c. These design parameters are given in percentages of chord length since the dimensions and positioning of the porpoise nose along the span vary because of the taper and twist of the aircraft wing.

Furthermore, the porpoise nose modification has only been implemented along a certain span of the wing forming a leading-edge bump. The porpoised bump of the wing was built between semi-wingspan ($b/2$) sections at 0.4 m and 1.8 m (i.e. between 20% and 90% of the semi-wingspan). To render the porpoised nose bump, 12 airfoil cross-sections cuts along the span were employed where the airfoil cross-section was modified only at 10 spanwise sections, as shown in Figure 7(a), excluding those at 0.4 m and 1.8 m which remained as the original MH61 airfoil. Subsequently, a volume blend was exerted from the original MH61 airfoil at 0.4 m along the porpoised cross sections until the original MH61 at 1.8 m to assure a smooth transition between spanwise sections and avoid blend overfitting as shown in Figure 7(b). Finally, to complement Figure 7, Table 2 presents the bump dimensioning along the span for future manufacturing specifications and Figure 7(c) shows the detail of the porpoise nose at the wingspan section of 0.6 m
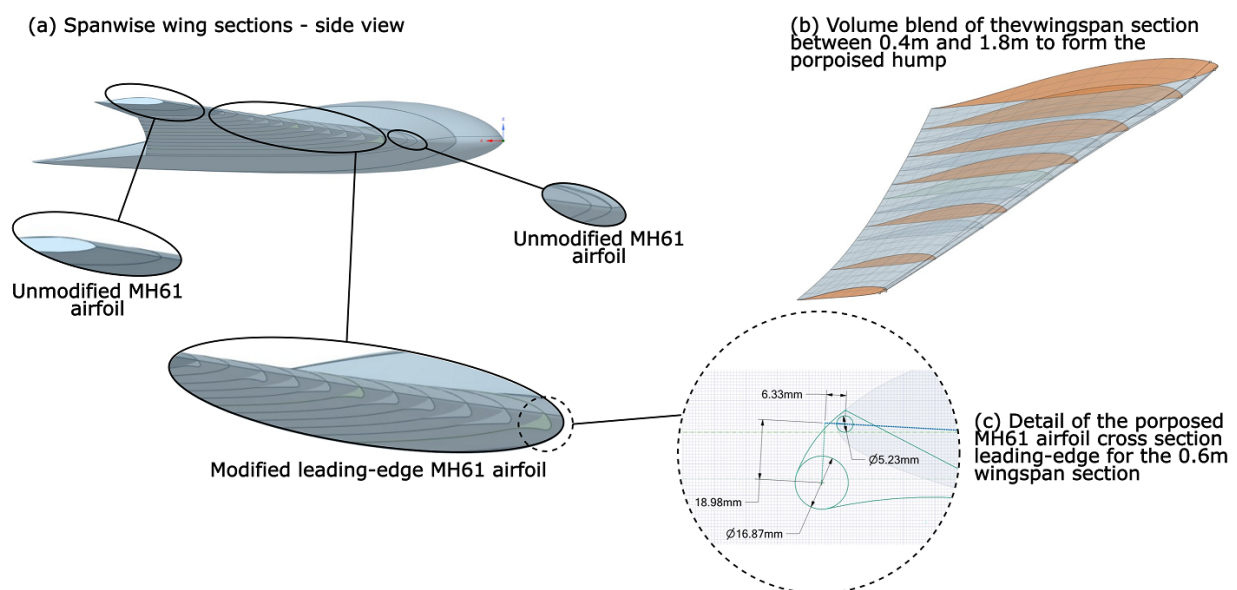

(a) Spanwise wing sections - side view

Unmodified MH61 airfoil

Unmodified MH61 airfoil

Modified leading-edge MH61 airfoil

(b) Volume blend of thevwingspan section between 0.4m and 1.8m to form the porpoised hump

6.33mm

Ø5.23mm

18.98mm

Ø16.87mm

(c) Detail of the porposed MH61 airfoil cross section leading-edge for the 0.6m wingspan section

Figure 7: Porpoise nose modification schematics

STALL DEVELOPMENT CONTROL

Table 2: Purpoise hump nose geometrical specifications

$b/2$ [m]	$b/2$ [%]	$\varnothing_{LE}$ [mm]	$\varnothing_N$ [mm]	d_N [mm]	L_N [mm]
0.4	0.20	–	–	–	–
0.6	0.30	5.26	16.87	19.98	6.33
0.7	0.35	4.95	15.56	17.51	5.83
0.8	0.40	4.65	14.31	16.09	5.36
0.9	0.45	4.34	13.13	14.77	4.92
1.0	0.50	4.04	12.03	13.53	4.51
1.1	0.55	3.73	10.99	12.36	4.12
1.2	0.60	3.43	10.00	11.25	3.75
1.3	0.65	3.13	10.17	10.17	3.39
1.4	0.70	2.82	9.13	9.13	3.04
1.5	0.75	2.52	7.19	8.09	2.69
1.6	0.80	2.21	6.75	7.59	2.53
1.8	0.90	–	–	–	–

with the corresponding dimensions. A model comparison between the original and porpoised wing is not shown since the porpoise nose bump is a subtle geometry modification that is negligibly noticed with respect to the original wing.

3.2.2 Aerodynamic Performance

Once the aircraft with porpoised wing was rendered, the same meshing parameters described in Section 2 for the medium-level grid were used to generate the mesh of the newly modified aircraft. The resulting mesh is not shown since the overall geometry modifications are subtle enough for them to not be properly appreciated when comparing the baseline configuration and the aircraft with the porpoised wing. Furthermore, the same CFD setup as that used in Section 2 for the aircraft in cruise conditions was employed for the aerodynamic analysis of the configuration with the porpoised wing.

Subsequently, an aerodynamic analysis at cruise conditions of the porpoised leading-edge wings was conducted and the results were compared to those of the baseline wing. Figure 8 shows the lift coefficient curve and the drag polar comparisons between the porpoised and original aircraft configurations. Figure 8(left) shows that the aircraft with the porpoised wing achieves larger lift coefficients at higher angles of attack where the leading-edge modification leads to an improvement of α_{Stall} by 4 deg up to 13 deg and an increment of 27.3% in $C_{L_{Max}}$ which resulted in a value of 1.0395.
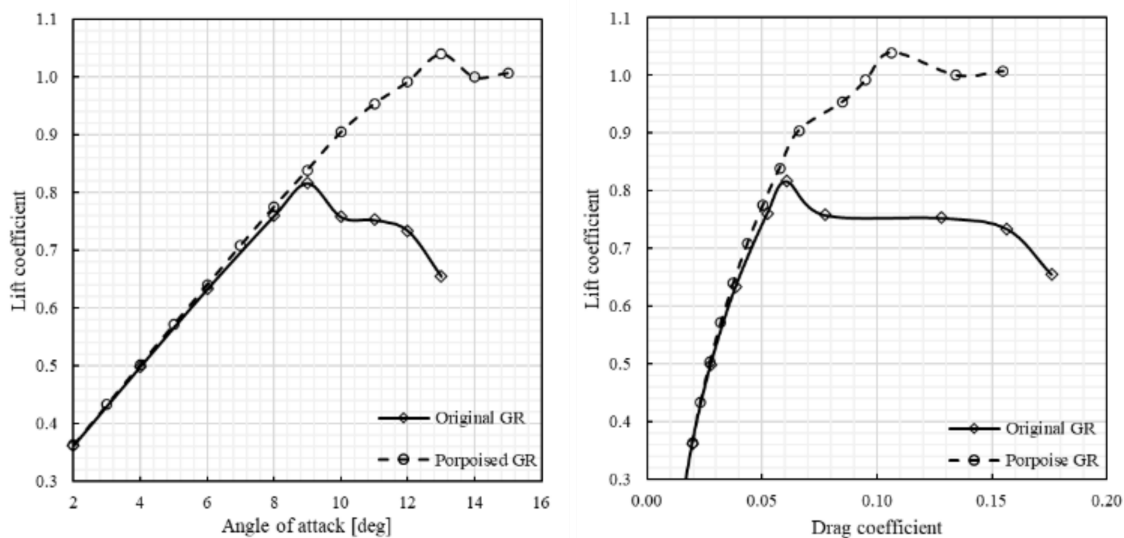

Figure 8: Comparison of aerodynamic performance between the baseline and porpoise wing designs. Lift curve (left) and drag polar (right)
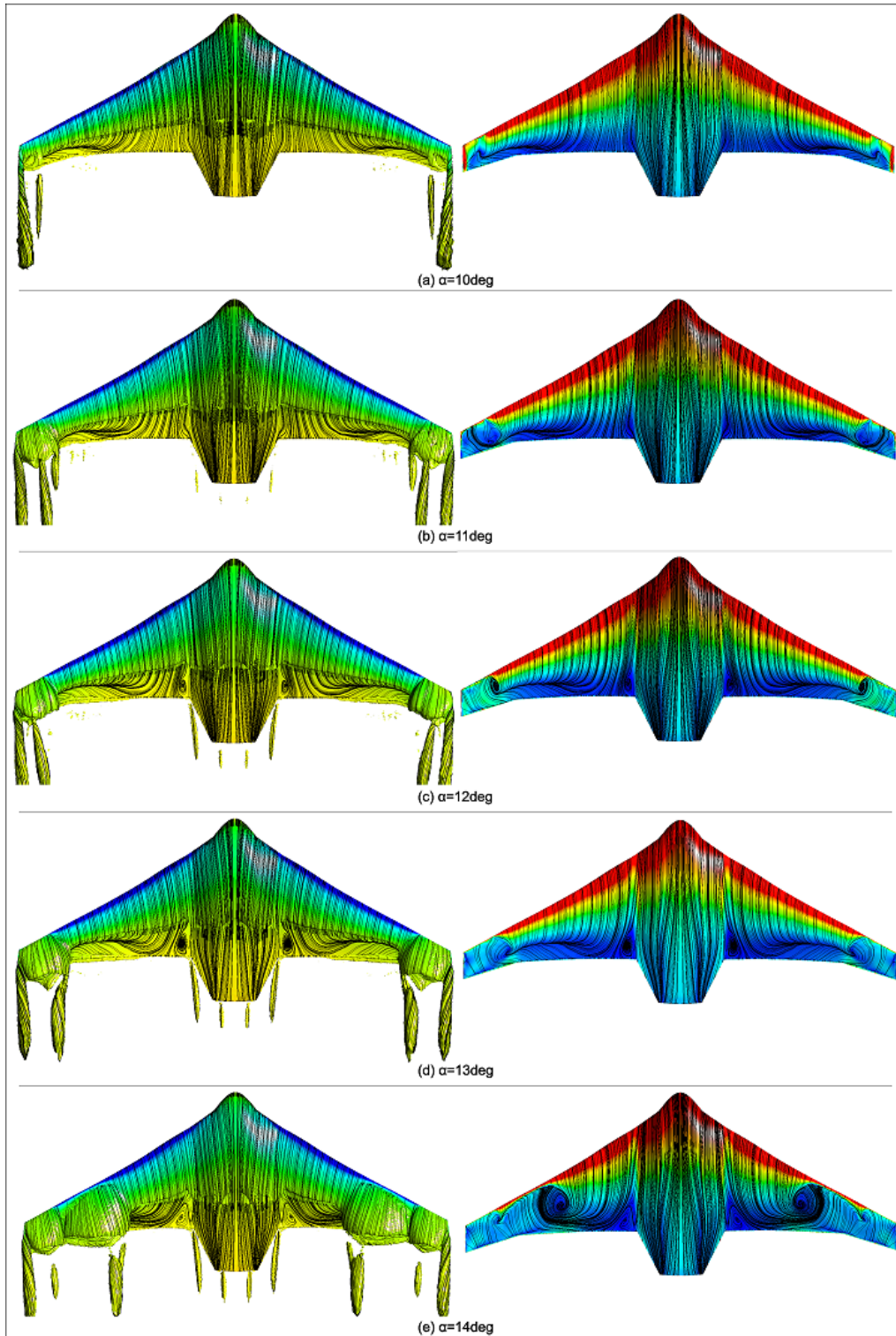
Figure 9: $\lambda_2 - criterion$ isosurfaces colored by pressure coefficient (left) and skin friction contours and lines (right) on the aircraft with the purpoised wing.

It's additionally observed in Figure 8(right) that there is a drag coefficient reduction when porpoised bump is employed on the wing which becomes considerable at higher lift coefficients. The latter is due to the reduction of pressure drag on the porpoised wing design at α where the baseline configuration is stalled and large-scale stall cells are produced on its wing. These are similar observations performed by Mohammed and Yadav[11] on the usage of the porpoise leading-edge modification on airfoils.

STALL DEVELOPMENT CONTROL

To understand the aerodynamic changes obtained for the aircraft with the porpoised wing, its flow separation development was studied through $\lambda_2 - isocontours$ colored by pressure coefficient and the skin friction coefficient contours and lines on the aircraft on a similar fashion previously performed for the baseline configuration. These numerical flow visualization results are shown in Figure 9 for angles of attack between 10 deg and 14 deg.

The numerical flow visualization of Figure 9(a) shows that there aren't large scale separation flow structures at $\alpha = 10\,deg$ on the porpoised wing and that there's only an incipient trailing edge flow separation starting at midspan of the wingspan section that becomes larger towards the wingtip, by assessing the skin friction contours and lines. This observation indicates that the flow separation development on the porpoised wing is different to that of the baseline aircraft configuration of Figure 6(top right), since modifying the leading edge mitigated the onset of stall cells at $\alpha = 10\,deg$. Another aspect of the flow to appreciate from Figure 9(a) is that the skin friction lines of the porpoised wing are considerably aligned to the streamwise direction showing no strong boundary layer crossflow close to the leading edge. This is a consequence of a higher downstream extent of acceleration of the flow produced by the porpoise bump on the upper surface compared to the baseline wing design, which in turn yield to a larger downstream and spanwise extent of the suction on the wing.

By observing Figure 9(a-d), it becomes noticeable that the wingspan sections at the wingtip, whose leading edge wasn't modified, are more prone to stall than those having the porpoise bump as the angle of attack increases from 10 deg. Therefore, it's observed in Figure 9(a-d) that the trailing edge flow separation increases faster with angle
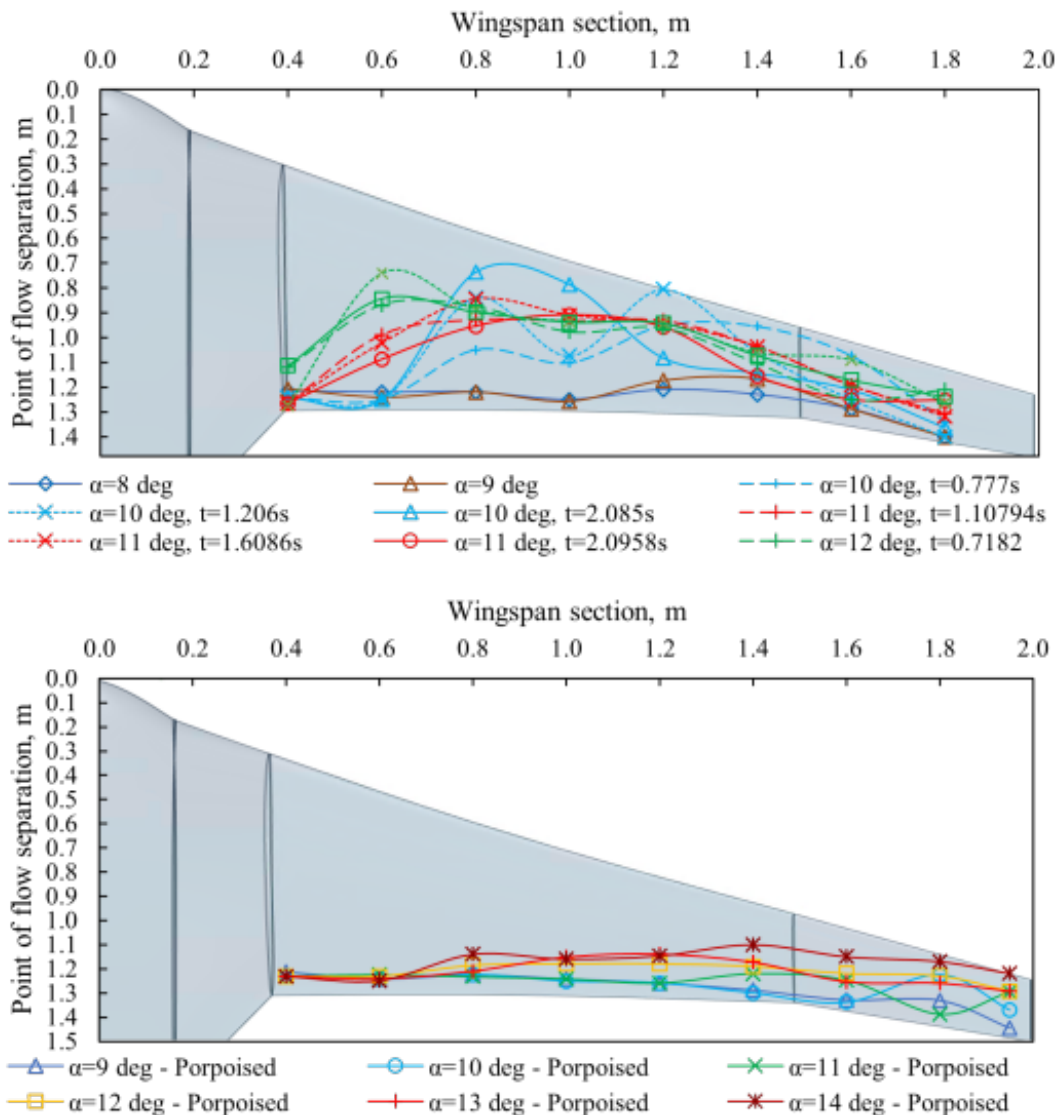

Figure 10: Comparison of the line of flow separation during and post-stall between the baseline (top) and porpoised wing design (bottom)

of attack at the wingtip forming an outboard stall cell. Consequently, the usage of a porpoise bump modification along a certain spanwise midspan extent produced a change on the stall development over the wing from an abrupt midspan leading-edge stall to an enforced moderate wingtip stall. Moreover, it's seen from Figure 9(a-d) that the flow acceleration at the leading edge of non-stalled wingspan sections is maintained and no boundary layer crossflow is observed from the skin friction lines topology.

An additional remark on how the flow separation develops on the porpoised wing is that it's observed from Figure 9 that as the angle of attack increases, the inboard trailing edge flow separation increases upstream and inboard along the span as the outboard stall cell grows inboards. Eventually, the porpoised wing configuration stalls at $\alpha = 14\ deg$ where a second midspan stall cell takes place when the adverse pressure gradient on the porpoised midspan wing sections has become strong enough to cause midspan leading edge flow separation as observed in Figure 9(e). Nonetheless, inboard wingspan sections are still stall resistant at this post-stall angle of attack.

To conclude the aerodynamic analysis of the porpoised leading-edge wing, Figure 10 shows the line of flow separation along the span of the baseline wing for α between 9 deg to 14 deg and that of the porpoised wing for α between 9 deg to 14 deg. Results of Fig. 10 (top) show that the line of flow separation of the baseline aircraft has an unsteady behavior after stall where the stall cell varies periodically its size along the span. By comparing both Figure 10(top) and (bottom), it's observed that the usage of the porpoise bump along a certain span region of the wing allows to control the stall development on the wing by enforcing a wingtip trailing-edge stall avoiding the unsteady and undesirable midspan leading-edge separation of the baseline wing design. The reason behind this change has been already explained previously, and these results are shown for future research on flow control on the porpoised wing where the point of flow separation becomes a relevant parameter of study such as in the case of using vortex generators to further control flow separation on the aircraft.

4. Conclusions

The aerodynamic analysis of the UAV under development at KTH was conducted numerically at cruise conditions using URANS with the Spalart-Allmaras turbulence model and stall of the UAV at cruise conditions was predicted at α_{Stall} equal to 9 deg for $C_{L_{Max}}$ of 0.8166.

The stall onset of the aircraft was identified numerically to occur due to the interaction between the wingtip vortex and the trailing edge separation region that produces a crossflow on the upper surface that simultaneously decreases the inertia of the boundary layer at midspan wing sections. Furthermore, the leading-edge geometry of the baseline configuration, simultaneously with the swept wing flow characteristics of the aircraft, produced a flow coalescence line at the leading edge due to a strong boundary layer cross flow at α_{Stall} which in turn makes the midspan wingspan sections prone to stall onset. These flow phenomena cause the trailing edge flow separation developed at low angles of attack to break into a large-scale, midspan stall cell that ensues the post-stall loss of lift.

The stall characteristics of the baseline are undesirable and a redesign of the leading-edge was performed to improve the flow acceleration at the leading edge and control the flow separation development. Hence, a bio-inspired LE modification was employed considering the optimum parameters for a porpoise whale nose estimated by Mohammed and Yadav [4]. This leading edge modification was employed within semiwingspan sections from 0.4 m to 1.8 m to generate a porpoised leading edge. The aerodynamics of the porpoised wing were studied numerically and the resulting α_{Stall} and $C_{L_{Max}}$ were estimated to be 13 deg and 1.0395, respectively. This corresponds to an increment of α_{Stall} by 4 deg and an improvement of $C_{L_{Max}}$ of 27%. Moreover, the usage of the porpoised bump increased the downstream extent of the suction regions of the wings and the velocity gradients of the boundary layer at the leading edge. This modification suppressed the undesirable leading-edge crossflow and enforced a wingtip, trailing edge stall on the porpoised wing.

Future work on flow control on the porpoised wing is currently ongoing at the Aeronautical Vehicles Unit at KTH Royal Institute of Technology focusing on the implementation of aerodynamically-shaped vortex generators to further control flow separation. The implementation of vortex generators on the aircraft strongly relies on the present work since these passive flow control devices only perform when the flow separation on the wing develops from the trailing edge, such as that attained for the porpoised wing aircraft. Nonetheless, an additional study about the optimization of the porpoise bump of the aircraft is further suggested since the geometrical parameters employed for the porpoise nose in this work were those attained for Mohammed and Yadav on a different wing.[11]

Finally, the stall development control of the aircraft implementing a porpoise nose modification might pose an interesting development into the improvement on the aerodynamic performance of BWB aircraft. Up to the author's knowledge, previous studies on flow control of BWB aircraft has been focused only on active flow control strategies given how flow separation develops in these type of aircraft causing an abrupt, leading-edge stall.

STALL DEVELOPMENT CONTROL

5. Acknowledgments

References

[1] S. Suewatanakul, A. Porcarelli, A. Olsson, H. Grimler, A. Chiche, R. Mariani, and G. Lindbergh. Conceptual design of a hybrid hydrogen fuel cell/battery blended-wing-body unmanned aerial vehicle – an overview. *Aerospace – MDPI*, 9(275):1–23, 2022.

[2] R. Mariani, S. Suewatanakul, S. Ghika, A. L. Penela, P. Wennaghe, and B. Zang. Wind tunnel test of a blended wing body unmanned aerial vehicle. 33rd Congress of the International Council of the Aeronautical Sciences, 2022.

[3] P. Kaparos, C. Bliamis, and K. Yakinthos. Conceptual design of a uav with vtol characteristics. AIAA Paper 2019-3137, American Institute of Aeronautics and Astronautics, June 2019.

[4] P. Dehpanah and A. Nejat. The aerodynamic design evaluation of a blended-wing-body configuration. *Aerospace Science and Technology*, 43:96–110, 2015.

[5] P. Panagiotou and K. Yakinthos. Parametric aerodynamic study of blended-wing-body platforms at low subsonic speeds for uav ppplications. AIAA Paper 2017-3737, American Institute of Aeronautics and Astronautics, June 2017.

[6] A.M. Pavlenko, B.Y. Zanin, and M.M. Katasonov. Features of flow around the flying wing model at various attack and slip angle. PROCEEDINGS OF THE XXV CONFERENCE ON HIGH-ENERGY PROCESSES IN CONDENSED MATTER, 2017.

[7] P. Dehpanah and A. Nejat. Aerodynamic design, analysis and validation of a small blended-wing-body unmanned aerial vehicle. *Aerospace–MDPI*, 9(36):1–18, 2022.

[8] J.H.M. Ribeiro, K. Taira, J. Neal, M. Amitay, A. Burtsev, and V. Theofilis. Wake dynamics of tapered wings. part i: a computational study. AIAA Paper 2023-2297, American Institute of Aeronautics and Astronautics, January 2023.

[9] J. Neal, B. Gares, M. Amitay, A. Burtsev, V. Theofilis J.H.M. Ribeiro, and K. Taira. Wake dynamics of tapered wings. part ii: an expreimental study. AIAA Paper 2023-2298, American Institute of Aeronautics and Astronautics, January 2023.

[10] J. Katz. *Race Car Aerodynamics - Designing for Speed*. Massachssets Bentley Publishers, 2003.

[11] M.A.R. Mohamed and R. Yadav. Flow separation control using the cetacean species nose design. *European Journal of Mechanics, B/Fluids*, 89:139–150, 2021.

[12] J.C. Lin. Review of research on low-profile vortex generators to control boundary-layer separation. *Progress in Aerospace Sciences*, 38(4–5):289–420, 2002.

[13] X. Li, K. Yang, and X. Wang. Experimental and numerical analysis of the effect of vortex generator height on vortex characteristics and airfoil aerodynamic performance. *Energies*, 12(959), 2019.

[14] R.M. Ma, U. Guven, and R. Yadav. Flow separation control of naca-2412 airfoil with bio-inspired nose. *Aircraft Engineering and Aerospace Technology*, 91:1058–1066, 2019.

[15] J. Katz. High lift wing design for race-car applications. Aerospace Technology Conference and Exposition, 1995.

[16] H. Strueber. The aerodynamic design of the a350 xwb-900 high lift system. 29th Congress of the International Council of the Aeronautical Sciences, 2024.

[17] Carylsue. The porpoise of echolocation. https://blog.education.nationalgeographic.org/2015/03/31/the-porpoise-of-echolocation/, 2015.

[18] M. Bakhtiari and H. Ghassemi. A 2.5d numerical study on open water hydrodynamic performance of a voith-schneider propeller. *Mechanics and Industry*, 20(6), 2019.

[19] P. Spalart and S. Allmaras. A one-equation turbulence model for aerodynamic flows. Aiaa paper, American Institute of Aeronautics and Astronautics, 1992.

[20] P. Catalano and M. Amato. An evaluation of rans turbulence modelling for aerodynamic applications. *Aerospace Science and Technology*, 7:493–509, 2003.

[21] Z. lyu and J.R.R.A. Martins. Aerodynamic design optimization studies of a blended-wing-body aircraft. *Journal of Aircraft*, 51(5):1604–1617, 2014.

[22] R.E.M. Nasir, A. Zurriati, and W. Wisnoe. Investigation on aerodynamic characteristics of baseline-ii e-2 blended wing-body aircraft with canard via computational simulation. THE 4TH INTERNATIONAL MEETING OF ADVANCES IN THERMOFLUIDS (IMAT 2011), 2011.

[23] Z.B. Celik, U. Ghia, P.J. Roache, C.J. Freitas, H. Coleman, and P.E. Raad. Procedure for estimation and reporting of uncertainty due to discretization in cfd applications. *Journal of Fluids Engineering, Transactions of the ASME*, 130(7), 2008.

[24] F. Goetten, D.f. Finger, M. Marino, C. Bil, M. Havermann, and C. Bruan. A review of guidelines and best practices for subsonic aer-odynamic simulations using rans cfd. Asian Pacific International Symposium on Aerospace Technology, 2019.

[25] C. Li, S. Zhu, Y.-L. Xu, and Y. Xiao. 2.5d large eddy simulation of vertical axis wind turbine in consideration of high angle of attack flow. *Renew Energy*, 51:317–330, 2013.

[26] J. Jeong and H. Fazle. On the identification of a vortex. *Journal of Fluid Mechanics*, 285:69–94, 1995.

[27] J.N. Dias. Nonlinear lifting-line algorithm for unsteady and post-stall conditions. AIAA Paper 2016-4164, American Institute of Aeronautics and Astronautics, 1992.